Revealing Cation Exchange Induced Phase Transformations in Multi-Elemental Chalcogenide Nanoparticles

Joel M.R. Tan, Mary Scott, Wei Hao, Tom Baikie, Christopher T. Nelson, Srikanth Pedireddy, Runzhe Tao, Xingyi Ling, Shlomo Magdassi, Timothy White, Shuzhou Li, Andrew M. Minor, Haimei Zheng and Lydia H. Wong

Supplementary figures

Role of dodecanethiol (DDT)

Firstly, we would like to address the source of the electron involved in the reaction. In our reaction, dodecanethiol (DDT), serves as both sulphur source and reduction agent in this reaction. Yang *et al* reported that DDT can act as a reduction agent (reaction of dodecanethiol and Se on the formation of CZTSSe nanoparticle) and form didodecyl disulphide (C_{12}-S-S-C_{12}) as by-product.[1] In addition, it was reported by Jasieniak *et al* that the dodecanethiol decompose to form dodecane while donating the sulphur to form sulfide compounds.[2]

Calculation of the chemical potential of Sn^{4+} ($\Delta\mu_{Sn}$)

As Sn^{4+} is the reactant promoting cationic exchange in these reactions, we focus on the chemical potential of Sn^{4+} ($\Delta\mu_{Sn}$) to predict the thermodynamic feasibility of the proposed reaction equation. For the proposed reactions (equations 1-3) to be thermodynamically feasible, the minimum $\Delta\mu_{Sn}$ required must be lower than the lowest theoretical calculated chemical potential of Sn^{4+} available (Sn in Cu_4SnS_4 crystal matrix). Under equilibrium conditions, the summation of the chemical potentials ($\Delta\mu_\alpha$) of the constituent elements (e.g Cu, Sn, S) in Cu_4SnS_4 (reduced unit cell) phase equals that of the theoretical calculated enthalpy of formation.

$$\Delta H_f \text{ (Cu}_4\text{SnS}_4\text{)} = 4\Delta\mu_{Cu} + \Delta\mu_{Sn} + 4\Delta\mu_S = -2.24 \text{ eV} \qquad \textbf{(S1)}$$

Therefore, based on the theoretical calculated enthalpy of formation of Cu_4SnS_4 (equation S1 and Supplementary Table 1), the lowest possible $\Delta\mu_{Sn}$ available is -2.24 eV (assuming $\Delta\mu_{Cu}$ and $\Delta\mu_S$ to be 0). Following on, the $\Delta\mu_{Sn}$ required for the spontaneous reaction of the three proposed reactions (equations 1 to 3) is summarized in Supplementary Table 2. In a typical enthalpy of reaction calculation, the enthalpy of reaction can be written as

$$\Delta H_{equation\ 1,2,3} = \sum \Delta H_{product} - \sum \Delta H_{reactant} \qquad \textbf{(S2)}$$

$$\Delta\mu_{Sn,equation\ 1,2,3} = \Delta\mu_{Sn,equilibrium} + \Delta H \qquad \textbf{(S3)}$$

$$\Delta H = C_p\ \Delta T + V(1 - \alpha T)\Delta p \qquad \textbf{(S4)}$$

The calculated minimum of $\Delta\mu_{Sn,equation\ 1}$ is -2.43 eV, $\Delta\mu_{Sn,equation\ 2}$ is 2.42 eV and $\Delta\mu_{Sn,equation\ S3}$ is -0.78 eV. However for $\Delta H_{equation\ 1,2,3}$ to be thermodynamically spontaneous ($\Delta H_{equation\ S1,2,3} < 0$), the minimum $\Delta\mu_{Sn,equation\ 1,2,3}$ calculated has to be less than -2.23 eV. Therefore, equation 1 is thermodynamically spontaneous while equation 2 and 3 are thermodynamically

non-spontaneous. These calculated trend is in good agreement with experimental data, which shows a need for higher temperature for equation 2 and 3 to complete its reaction. From equation **S4**, where ΔH is the change in internal energy, C_p is the heat capacity constant of the solvent, ΔT is the change in temperature, V is the volume of the reaction solution, α is the coefficient of thermal expansion and Δp is the change in pressure. As the temperature increases, the thermal energy increases $\Delta \mu_{Sn}$. When $\Delta \mu_{Sn}$ is higher than the minimum required $\Delta \mu_{Sn, equation\ 2,3}$, the reaction then becomes spontaneous.

Calculation of the chemical potential of Zn²⁺ ($\Delta \mu_{Zn}$)

To explain the sequential observations, the thermodynamics of various reaction processes have to be verified. As Zn^{2+} is the reactant promoting cationic exchange in **reaction 5**, we focus on the chemical potential of Zn^{4+} ($\Delta \mu_{Zn}$) to predict the thermodynamic feasibility of the proposed reaction equation. In equilibrium conditions, the chemical potentials of the constituent elements in Cu_2ZnSnS_4 (reduced unit cell) phase must satisfy the following to form the desired crystal.
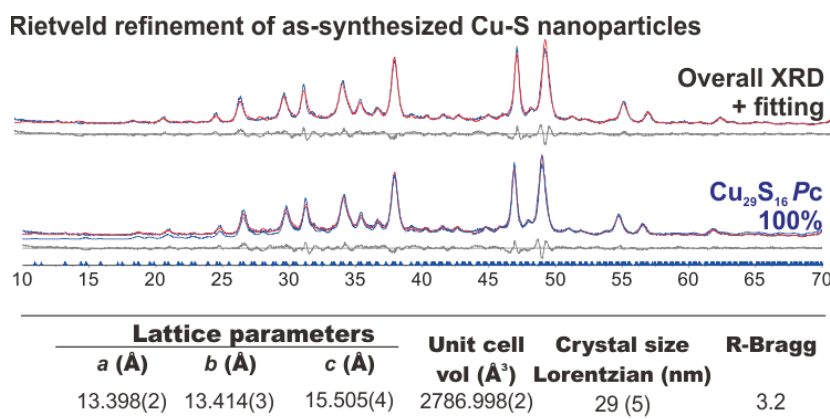
$$\Delta H_f\ (Cu_2ZnSnS_4) = 2\Delta \mu_{Cu} + \Delta \mu_{Zn} + \Delta \mu_{Sn} + 4\Delta \mu_S = -3.67\ \text{eV} \qquad \textbf{(S5)}$$

Based on the theoretical calculated enthalpy formation of Cu_2ZnSnS_4 (**equation S5**), $\Delta \mu_{Zn}{}^+$ in the reaction solution follows the lowest possible chemical potential energy of Zn (Zn in Cu_2ZnSnS_4 crystal matrix) available, which is -3.67 eV (assuming $\Delta \mu_{Cu}$, $\Delta \mu_S$ and $\Delta \mu_{Sn}$ to be 0). However, $\Delta \mu_{Zn, equation\ 8}$ is calculated to be -1.78 eV (Supplementary Table 2) which is higher than theoretical calculated chemical potential available of -3.67 eV (Supplementary Table 1), hence thermodynamically nonspontaneous.
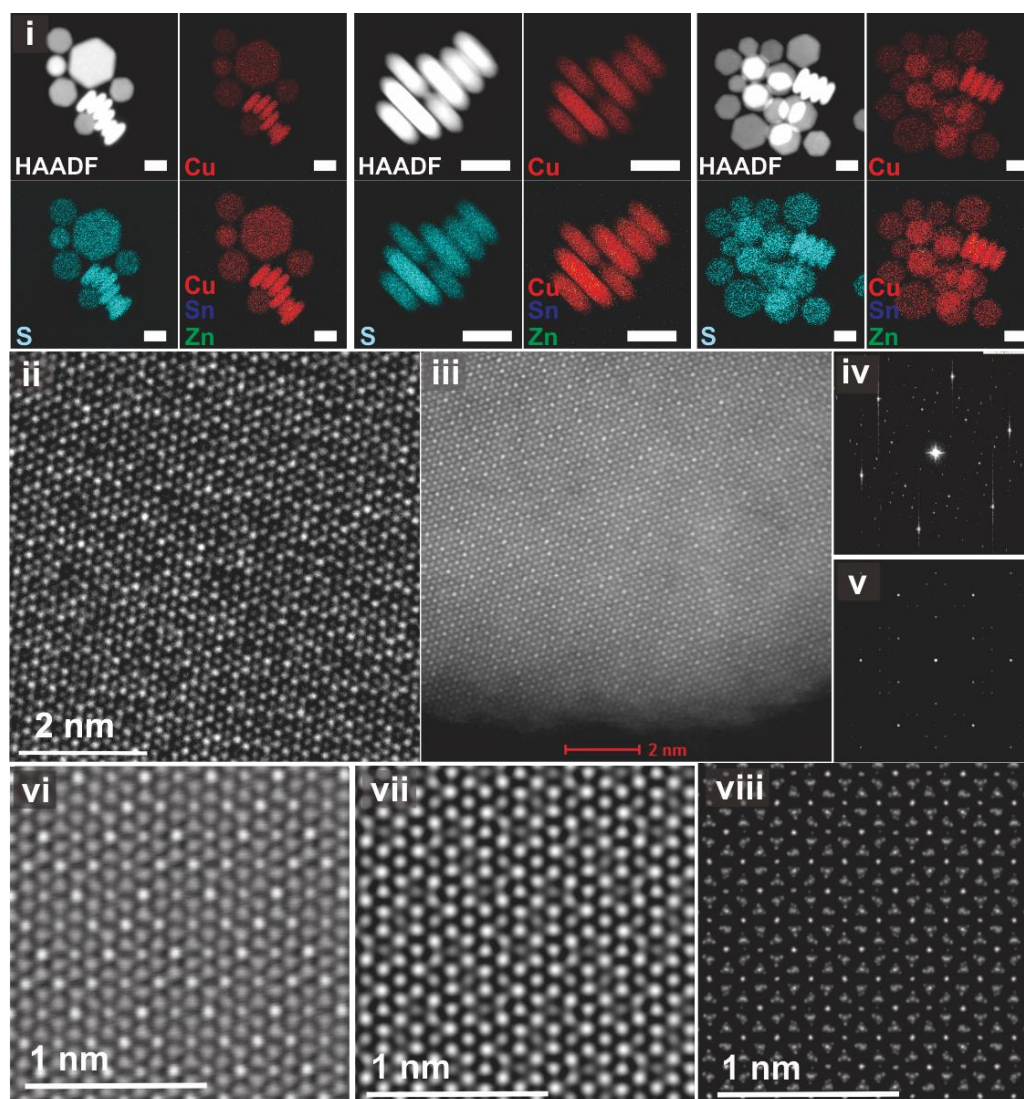
Supplementary Figure 1| (i) Elemental mapping of as-synthesized Cu-S nanoparticles on various TEM carbon grid spots. Scale bar is 30 nm. **(ii)** HR-BF imaging, **(iii)** HR-HAADF imaging, **(iv)** FFT image of **(iii)**, **(v)** JEMS simulated TEM diffraction pattern along <100> zone axis. **(vi)** CRISP-treated HR-HAADF image, **(vii)** JEMS simulated HR-HAADF image along <100> zone axis, and **(viii)** JEMS simulated crystal potential along <100> zone axis.

$Cu_{29}S_{16}$ nanoplates of ~30 nm are obtained as starting nanoparticles for subsequent reaction. As shown in **SF1ii&iii**, the ordered hexagonal arrangement of atomic columns correspond to the <100> zone axis. The zone axis is also verified by matching the FFT (**SF1iv**) of SF1iii with simulated FFT of <100> zone axis of $Cu_{29}S_{16}$ phase (**SF1v**). In addition, as the HR-HAADF image shows ordered bright spots, we did a simulation of a HR-HAADF image of <100> zone axis of $Cu_{29}S_{16}$ phase (**SF1vi-viii**) to verified that the bright spots are due to the presence of heavier sulfur anions in the atomic columns while the dull spot are due to the lack of heavier sulfur anions (only Cu ions) in the atomic columns.

Rietveld refinement of as-synthesized Cu-S nanoparticles

Lattice parameters			Unit cell	Crystal size	R-Bragg
a (Å)	b (Å)	c (Å)	vol (Å³)	Lorentzian (nm)	
13.398(2)	13.414(3)	15.505(4)	2786.998(2)	29 (5)	3.2

Supplementary Figure 2| Rietveld refinement of XRD pattern of as-synthesized $Cu_{58}S_{32}$ nanoparticles.
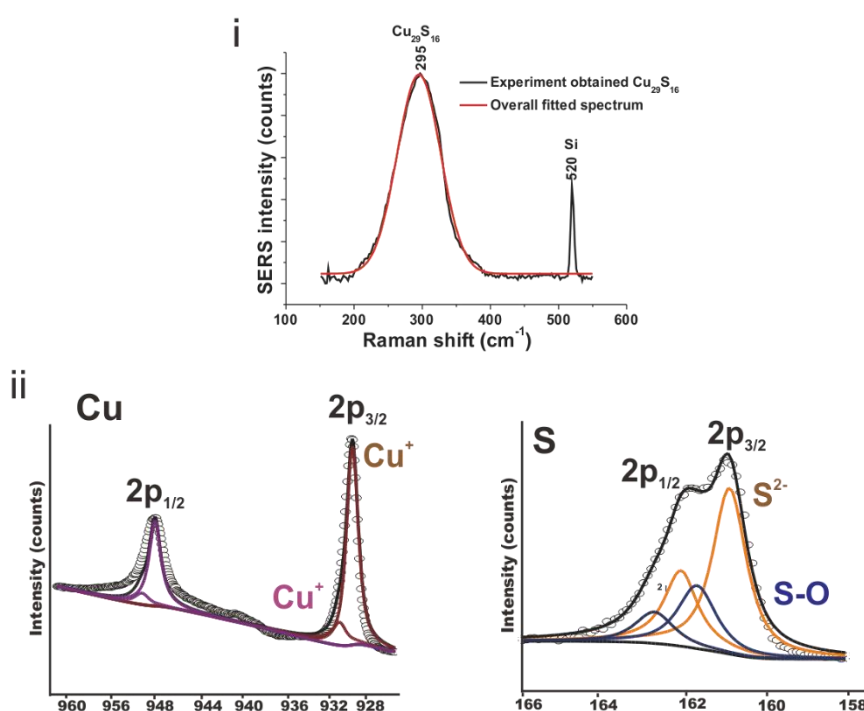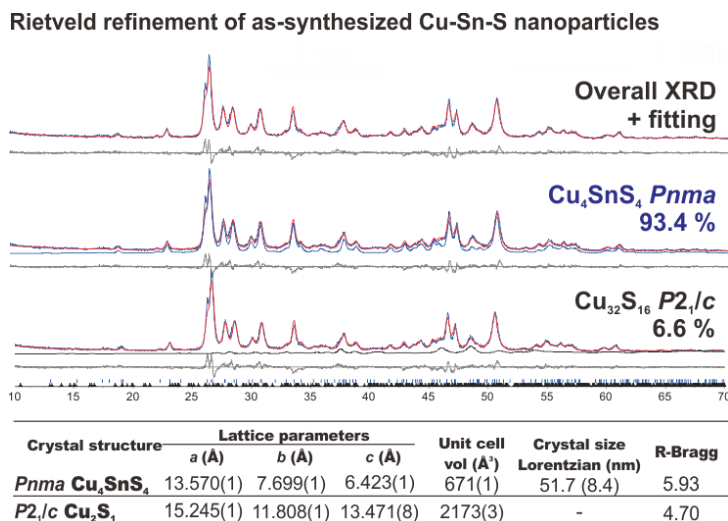

Supplementary Figure 3| peak fitting of SERS spectrum and **(ii)** XPS characterization of Cu-S nanoparticles.

Rietveld refinement (**SF2**) of as-synthesized Cu-S nanoplates shows good fitting to *Pc* $Cu_{29}S_{16}$ with a fitted lattice parameters of *a*=13.40 Å, *b*=13.41 Å, *c*=15.51 Å. The fitted crystal size of ~30 nm correspond well to observe average crystal size from TEM. SERS characterization (**SF3i**) of $Cu_{29}S_{16}$ shows a peak at ~295 cm⁻¹, while XPS characterization shows the presence of both Cu⁺ and Cu²⁺ in the nanoparticles (**SF3ii**) ($Cu_3^{2+}Cu_{26}^+S_{16}^{2-}$).

5
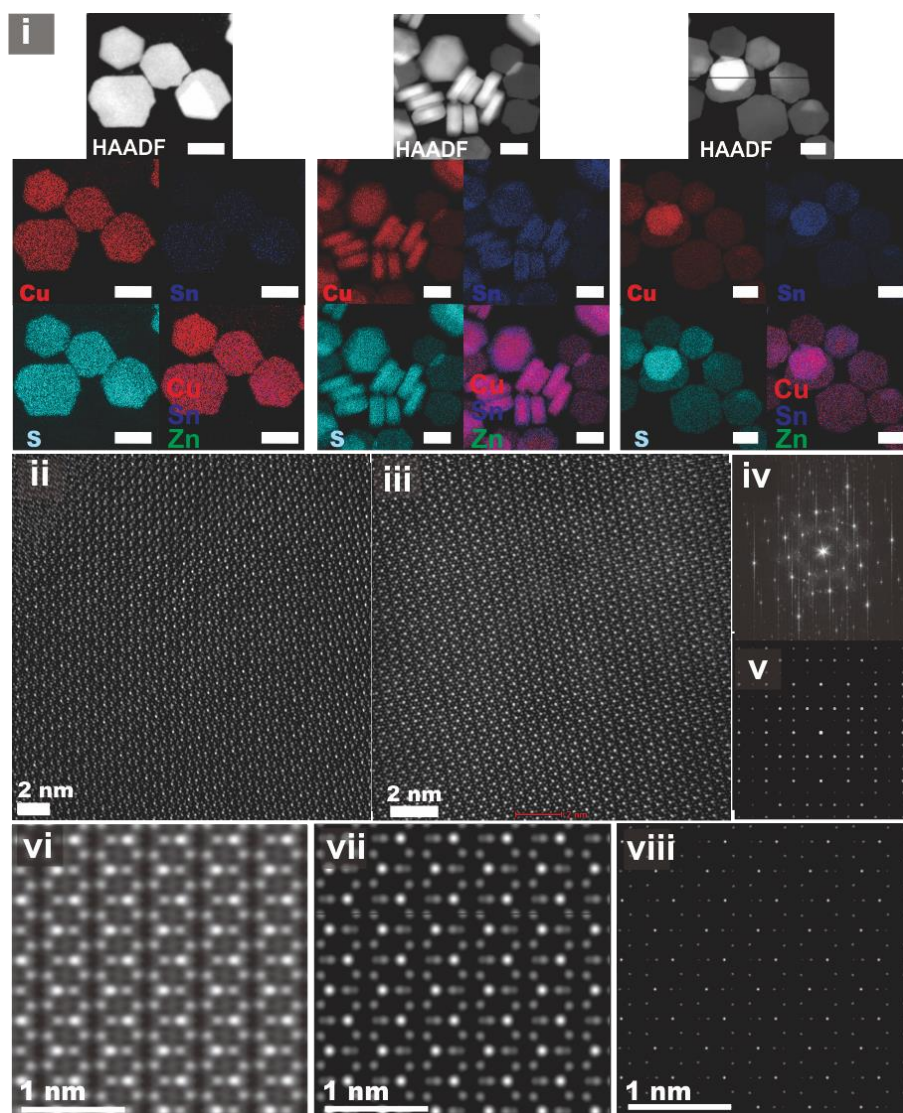
Supplementary Figure 4| (i) Elemental mapping of as-synthesized Cu-Sn-S nanoparticles on various TEM carbon grid spots. Scale bar is 30 nm. **(ii)** HR-BF imaging, **(iii)** HR-HAADF imaging, **(iv)** FFT image of **(iii)**, and **(v)** JEMS simulated TEM diffraction pattern along <100> zone axis. **(vi)** CRISP-treated HR-HAADF image, **(vii)** JEMS simulated HR-HAADF image along <001> zone axis, **(viii)** JEMS simulated crystal potential along <001> zone axis.

When Sn^{4+} is added into a dispersion of $Cu_{29}S_{16}$ and allowed to react for 60 mins at 230 °C, Cu_4SnS_4 nanoplates of ~40-60 nm are obtained. As shown in **SF4ii&iii**, the ordered hexagonal arrangement of atomic columns correspond to the <100> zone axis. The zone axis is also verified by matching the FFT (**SF4iv**) of SF1iii with simulated FFT of <100> zone axis of Cu_4SnS_4 phase (**SF4v**). In addition, as the HR-HAADF image shows ordered bright spots, we did a simulation of a HR-HAADF image of <100> zone axis of Cu_4SnS_4 phase (**SF4vi-viii**) to verified that the bright spots are due to the presence of heavier Sn ions.

Rietveld refinement of as-synthesized Cu-Sn-S nanoparticles

Overall XRD + fitting

Cu₄SnS₄ Pnma 93.4 %

Cu₃₂S₁₆ P2₁/c 6.6 %

Crystal structure	Lattice parameters			Unit cell vol (Å³)	Crystal size Lorentzian (nm)	R-Bragg
	a (Å)	b (Å)	c (Å)			
Pnma **Cu₄SnS₄**	13.570(1)	7.699(1)	6.423(1)	671(1)	51.7 (8.4)	5.93
P2₁/c **Cu₂S₁**	15.245(1)	11.808(1)	13.471(8)	2173(3)	-	4.70

Supplementary Figure 5| Rietveld refinement of XRD pattern of as-synthesized Cu-Sn-S nanoparticles.
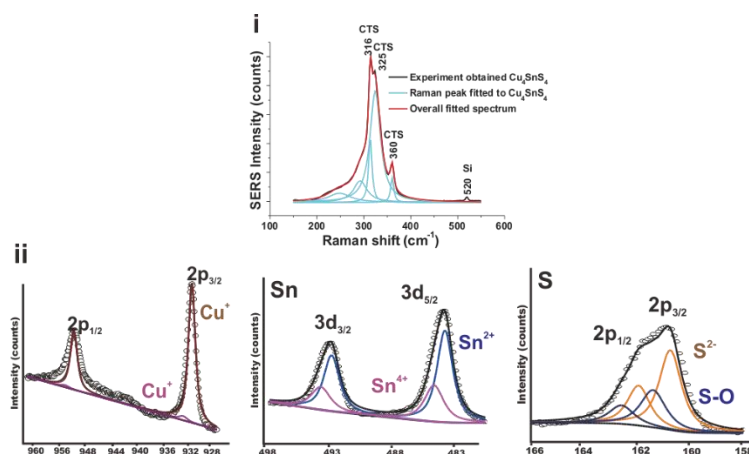
Supplementary Figure 6| (i) Peak fitting of SERS spectrum and **(ii)** XPS characterization of as-synthesized Cu-Sn-S nanoparticles.

Rietveld refinement (**SF5**) of as-synthesized Cu-Sn-S nanoplates shows good fitting to *Pnma* Cu₄SnS₄ with a fitted lattice parameters of a=13.57 Å, b=7.70 Å, c=6.42 Å. The fitted crystal size of ~52 nm correspond well to observe average crystal size from TEM (**SF4**). SERS characterization (**SF6i**) of Cu₄SnS₄ shows a peak at ~295 cm⁻¹, while XPS characterization (**SF6**) shows the presence of both Cu⁺ and Cu²⁺, Sn²⁺ and Sn⁴⁺ ions in the nanoparticles (**SF6ii**). The presence of Sn²⁺ could be due to the reduction of Sn⁴⁺ by DDT. As the standard reduction potential of Cu²⁺ to Cu⁺ (+0.159) and Sn⁴⁺ to Sn²⁺ (+0.150) is similar, the formation of Sn²⁺ as shown in our XPS could be due to the reduction by DDT (J. Am. Chem. Soc. 2014, 136, 16277-16284). We understand from the paper by Manna (J. Am. Chem. Soc. 2014, 136, 16277-16284.) that the presence of Sn²⁺ will lead to the formation of binary SnS instead of ternary Cu-Sn-S, however from our XRD, SERS and EDX, there is no detectable presence of SnS phase. From our characterization (**SF4-SF6**), we only observe Cu₄SnS₄ phase.

Elemental mapping: Time-growth study of $Cu_{29}S_{16}$ to Cu_4SnS_4 0.22 mmole Sn^{4+}
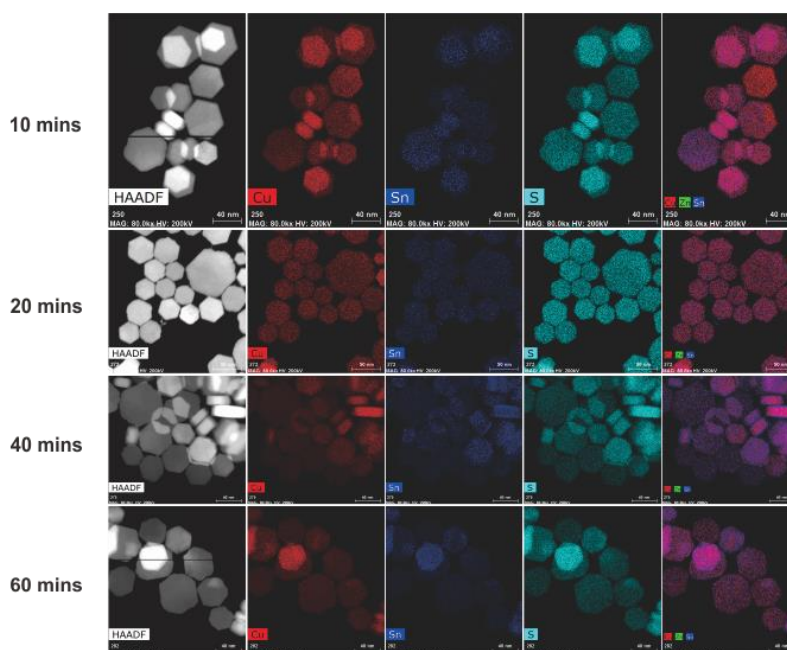
|	(atom %)		
	Cu	**Sn**	**S**
10 mins	52.7 ± 4.9	7.8 ± 2.4	39.5 ± 3.8
20 mins	42.5 ± 3.9	13.1 ± 4.0	44.4 ± 4.2
40 mins	42.1 ± 3.9	13.8 ± 4.2	44.1 ± 4.1
60 mins	43.3 ± 4.0	12.7 ± 3.7	44.0 ± 4.1

Supplementary Figure 7| Elemental mapping of nanoparticles obtained during ex-situ study during the growth of Cu_4SnS_4 from $Cu_{29}S_{16}$ at 10, 20, 40 and 60 mins.

Reaction aliquots are extracted at fixed time interval to analyst the change in element composition during growth. As shown in **SF7**, nanoparticles extracted at 10 mins shows a relative element composition of 6.6:1:5 (Cu:Sn:S). When the reaction is allowed to proceed, the amount of Sn increases to 4:1:4 (Cu:Sn:S) at 20 mins and the elemental composition does not change much from 20 to 60 mins.
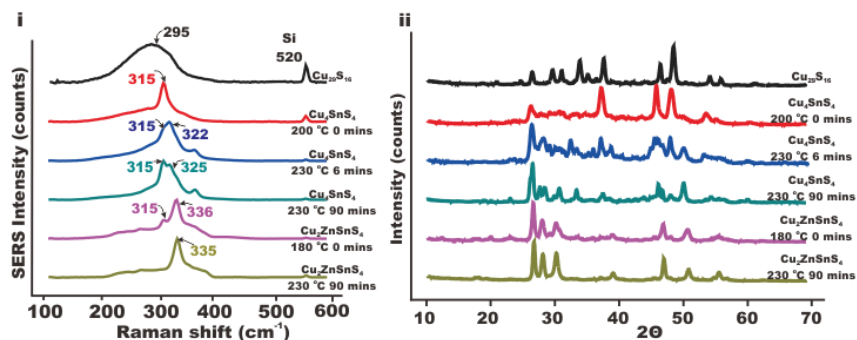
Supplementary Figure 8| (i) SERS spectrum and **(ii)** XRD characterization of as-synthesized $Cu_{29}S_{16}$ nanoparticles (Black line), addition of 0.22 mmol Sn^{4+} to $Cu_{29}S_{16}$ nanoparticle solution and react at 200 °C for 0 min (Cu_4SnS_4 200°C for 0 min Red line), 230°C for 6 mins (Cu_4SnS_4 230°C for 6 mins Blue line) and 230 °C for 60 mins (Cu_4SnS_4 Green line), addition of 0.22 mmol Zn^{2+} to Cu_4SnS_4 nanoparticle colution and react at 180 °C for 0 min (Cu_2ZnSnS_4 180 °C for 0 min Magenta line) and 230 °C for 90 mins (Cu_2ZnSnS_4 Brown line); Quenching of reaction immediately (0 min).

Aliquots extracted at selected time interval for the reaction [(1)Cu-S + Sn → Cu-Sn-S, (2) Cu-Sn-S + Zn → Cu-Zn-Sn-S] are characterized by surface enhanced Raman scattering (SERS) spectroscopy. As shown in **SF8**, the starting $Cu_{29}S_{16}$ nanoparticles shows a broad peak at 295 cm^{-1}, when Sn^{4+} is added into $Cu_{29}S_{16}$ and the reaction allowed to reach 200 °C, the peak shift to 315 cm^{-1}. The shift in the Raman peak is due to the incorporation of Sn^{4+} into Cu-S crystal matrix as shown in **SF9** where Cu_4SnS_4 and $Cu_{31}S_{16}$ phases are observed. When the reaction is allow to heat up to 230 °C and react for 6mins, two peaks are observed (315 and 322 cm^{-1}). As the reaction is allowed to proceed for 90 mins, the SERS spectra did not change which show two peaks at (315 and 325 cm^{-1}). When Zn^{2+} is added to Cu_4SnS_4 nanoparticles and allowed to heat up to 180 °C, the peak at 325 cm^{-1}shifted to 336 cm^{-1}while the peak intensity at 315 cm^{-1} decreases. After reacting for 90 mins at 230 °C a peak at 335 cm^{-1} is observed which correspond to CZTS phase.
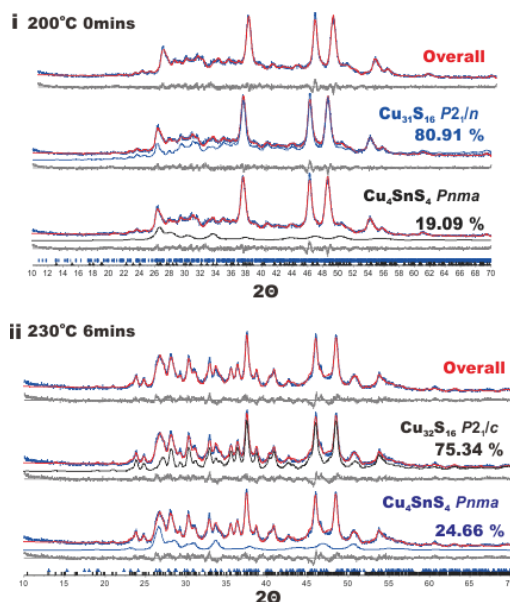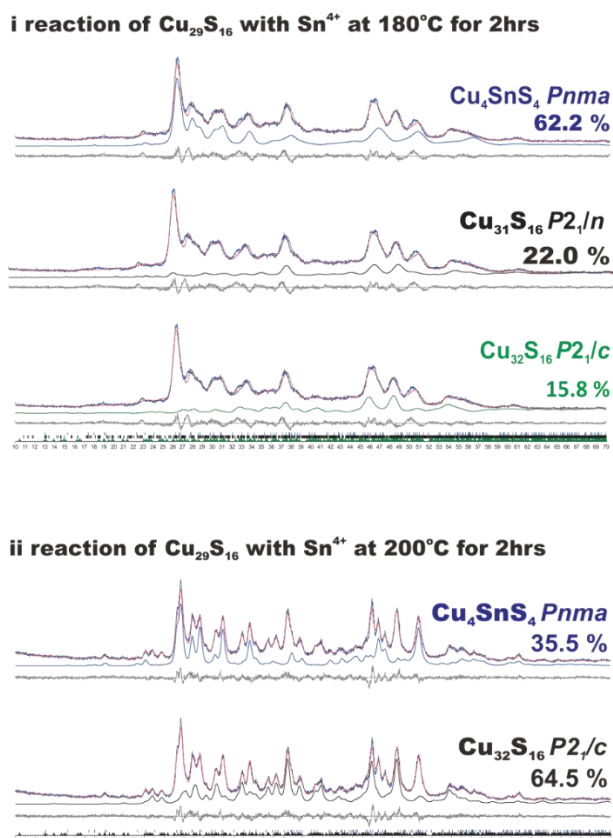

Supplementary Figure 9| Rietveld refinement of XRD diffraction patterns of **(i)** 200ºC for 0 mins and **(ii)** 230ºC for 6 mins after addition of Sn^{4+} into $Cu_{29}S_{16}$ nanoparticles solution
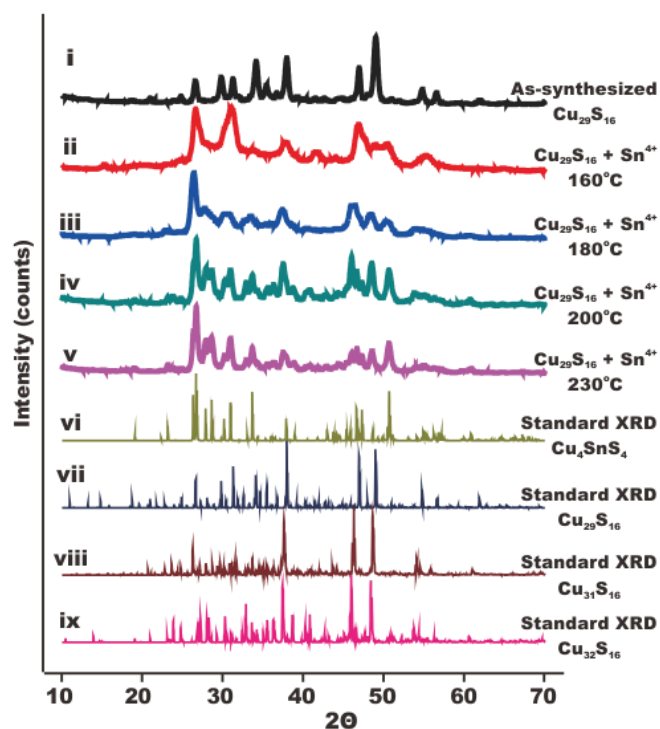
Supplementary Figure 10| Phases presence at fixed temperature interval. XRD spectrum of as-synthesized CTS nanoparticles after addition of Sn^{4+} into $Cu_{29}S_{16}$ nanoparticles solution, heated and immediately quenched upon reaching targeted temperature. **(i)** As-synthesized $Cu_{29}S_{16}$ nanoparticles showing crystal phase of *Pc* $Cu_{29}S_{16}$. Solution quenched at **(ii)** 160 °C showing crystal phase of *Pc* $Cu_{29}S_{16}$ + *Pnma* Cu_4SnS_4, **(iii)** 180 °C showing crystal phase *Pc* $Cu_{29}S_{16}$ + $P12_1c1$ $Cu_{31}S_{16}$ + *Pnma* Cu_4SnS_4, **(iv)** 200 °C showing crystal phase of $P12_1c1$ $Cu_{31}S_{16}$ + *Pmna* Cu_4SnS_4, **(v)** 230 °C showing crystal phase $P12_1n1$ $Cu_{32}S_{16}$ + *Pmna* Cu_4SnS_4. Standard XRD of **(vi)** *Pnma* Cu_4SnS_4, **(vii)** *Pc* $Cu_{29}S_{16}$, **(viii)** $P12_1c1$ $Cu_{31}S_{16}$ and **(ix)** $P12_1n1$ $Cu_{32}S_{16}$.

To determine possible intermediate phase during the growth, separate reaction ($Cu_{29}S_{16}$ + Sn^{4+}) are carried out with each reaction stopped (quenching in cold water bath) immediately when reaction temperature reached 160 °C, 180 °C, 200 °C and 230 °C respectively. As-synthesized $Cu_{29}S_{16}$ nanoparticles show crystal phase of *Pc* $Cu_{29}S_{16}$ (**SF10i**). Nanoparticles obtained from solution quenched at 160 °C (**SF10ii**) shows crystal phase of *Pc* $Cu_{29}S_{16}$ + *Pnma* Cu_4SnS_4, while the nanoparticles quenched at 180 °C (**SF10iii**) shows crystal phase of *Pc* $Cu_{29}S_{16}$ + $P12_1c1$ $Cu_{31}S_{16}$ + *Pnma* Cu_4SnS_4. When the reaction is quenched at 200 °C (**SF10iv**), the diffractogram shows crystal phase of $P12_1c1$ $Cu_{31}S_{16}$ + *Pmna* Cu_4SnS_4, while nanoparticles quenched at 230 °C (**SF10v**) showing crystal phase $P12_1n1$ $Cu_{32}S_{16}$ + *Pmna* Cu_4SnS_4. From the diffractograms, no other Cu-Sn-S phase is observed.

i reaction of Cu$_{29}$S$_{16}$ with Sn^{4+} at 180°C for 2hrs

Cu$_4$SnS$_4$ *Pnma*
62.2 %

Cu$_{31}$S$_{16}$ *P2$_1$/n*
22.0 %

Cu$_{32}$S$_{16}$ *P2$_1$/c*
15.8 %

ii reaction of Cu$_{29}$S$_{16}$ with Sn^{4+} at 200°C for 2hrs

Cu$_4$SnS$_4$ *Pnma*
35.5 %

Cu$_{32}$S$_{16}$ *P2$_1$/c*
64.5 %

Supplementary Figure 11| Rietveld refinement of XRD pattern obtained from nanoparticles after reacting Cu$_{29}$S$_{16}$ nanoparticles with Sn^{4+} at **a.** 180 °C for 2 hrs and **b.** 200 °C for 2 hrs

To proof that 230 °C is the minimum temperature for complete conversion of Cu$_{29}$S$_{16}$ to Cu$_4$SnS$_4$, longer reaction time of 120 mins (instead of 60 mins) are ran for lower reaction temperature of 180 °C and 200 °C. From the Rietveld refinement (**SF11**) it is observed in both 180 °C and 200 °C, there are unreacted Cu-S phase observed.
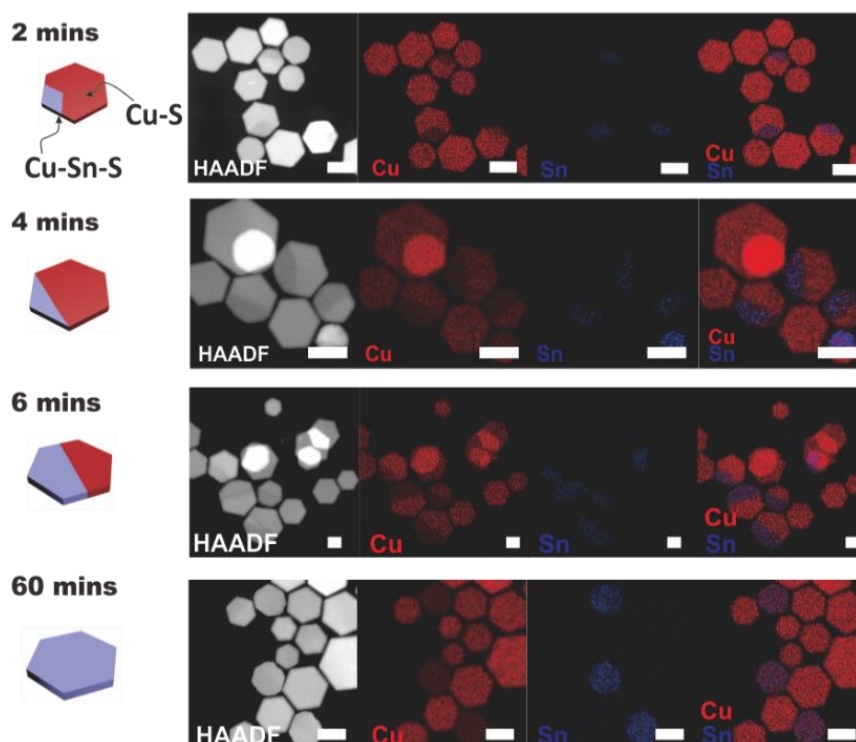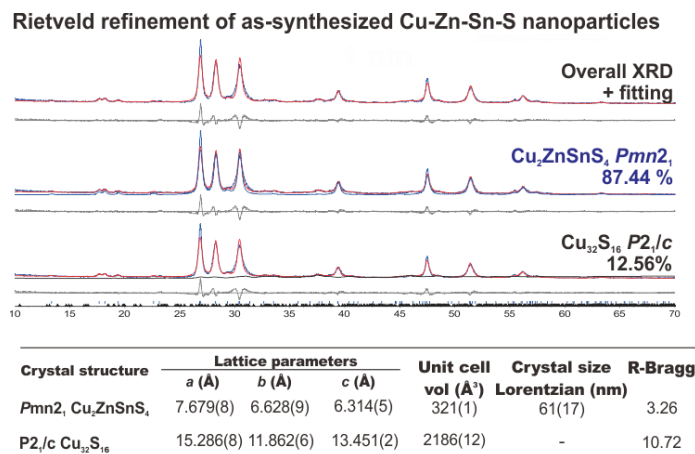
Supplementary Figure 12| Elemental mapping and HR-TEM of nanoparticles obtained during ex-situ study of Cu_4SnS_4 nanoparticles grown from $Cu_{29}S_{16}$ using 0.057 mmol Sn^{4+} **(quarter)**. Elemental distribution change occurring across time 2, 4, 6 and 60 mins with pictorial illustration. Scale is 30 nm.

When the amount of Sn^{4+} is reduced during the reaction of Cu-S + Sn → Cu-Sn-S, it is observed that 2 separate nanoparticles population (Cu-S and Cu-Sn-S) are obtained. To understand the growth mechanism, aliquots are extracted at fixed time interval. Based on EDX mapping, we are able to obtain a relative 2D elemental distribution map. The difference in signal intensity (colour intensity/contrast) shows the difference in the amount of element present (contrast is within the same element). Small Cu-Sn-S rich phase (**SF12 2mins**) are growing on Cu-S rich nanoparticles, while Cu-S nanoparticles size have increased to ~40-50 nm. As the reaction is allowed to proceed, larger Cu-Sn-S rich phase can be seen on the hetero-nanoparticles (Cu-S/Cu-Sn-S) **(SF12 2-6 mins)**. This shows that more Sn have diffused into the nanoparticles. After 60 mins of reaction, 2 separate nanoparticles population (Cu-S and Cu-Sn-S) are obtained.
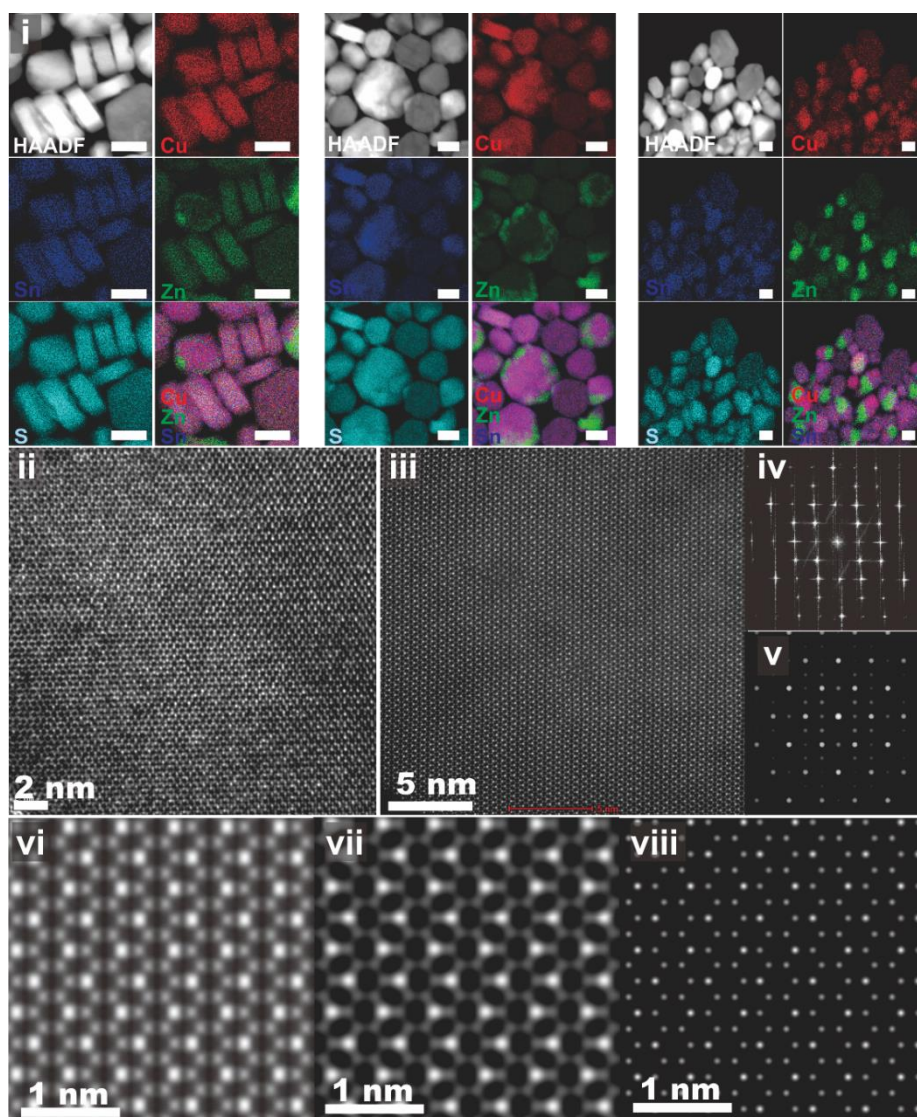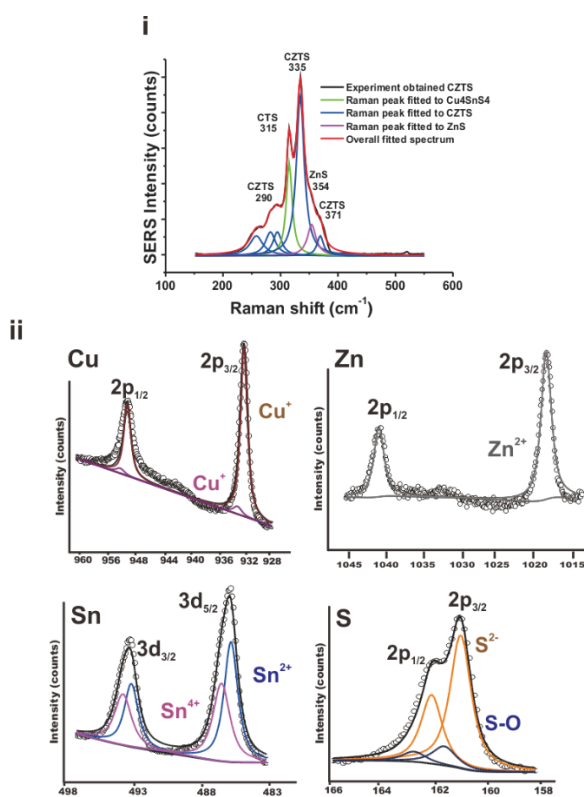
Supplementary Figure 13| (i) Elemental mapping of as-synthesized Cu-Zn-Sn-S nanoparticles on various TEM carbon grid spots. Scale bar is 30 nm. **(ii)** HR-BF imaging, **(iii)** HR-HAADF imaging, **(iv)** FFT image of **(iii)**, and **(v)** JEMS simulated TEM diffraction pattern along <001> zone axis. **(vi)** CRISP-treated HR-HAADF image, **(vii)** JEMS simulated HR-HAADF image along <001> zone axis, **(viii)** JEMS simulated crystal potential along <001> zone axis.

Cu_2ZnSnS_4 nanoplates of ~40-90 nm are obtained. As shown in **SF13ii&iii**, the ordered hexagonal arrangement of atomic columns correspond to the <001> zone axis. The zone axis is also verified by matching the FFT (**SF13iv**) of SF1iii with simulated FFT of <001> zone axis of Cu_2ZnSnS_4 phase (**SF13v**). In addition, as the HR-HAADF image shows ordered bright spots, we did a simulation of a HR-HAADF image of <001> zone axis of Cu_2ZnSnS_4 phase (**SF13vi-viii**) to verified that the bright spots are due to the presence of heavier Sn ions.

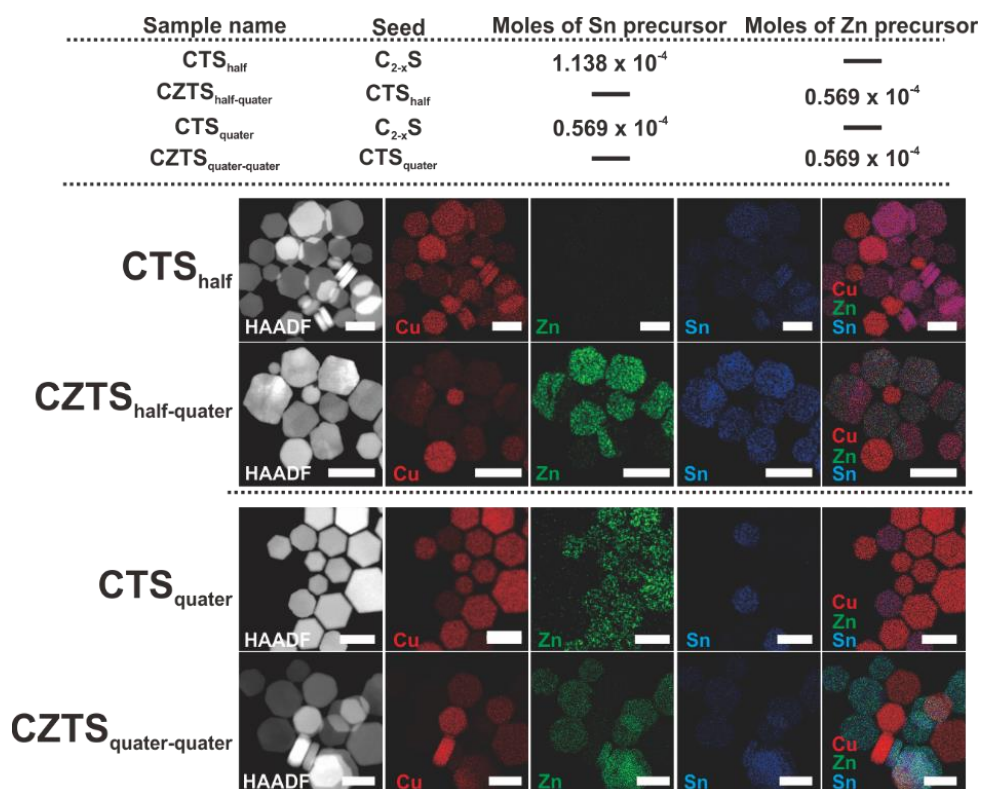**Rietveld refinement of as-synthesized Cu-Zn-Sn-S nanoparticles**

Crystal structure	Lattice parameters			Unit cell vol (Å³)	Crystal size Lorentzian (nm)	R-Bragg
	a (Å)	b (Å)	c (Å)			
Pmn2₁ Cu₂ZnSnS₄	7.679(8)	6.628(9)	6.314(5)	321(1)	61(17)	3.26
P2₁/c Cu₃₂S₁₆	15.286(8)	11.862(6)	13.451(2)	2186(12)	-	10.72

Supplementary Figure 14| Rietveld refinement of XRD pattern of as-synthesized Cu₂ZnSnS₄ nanoparticles.
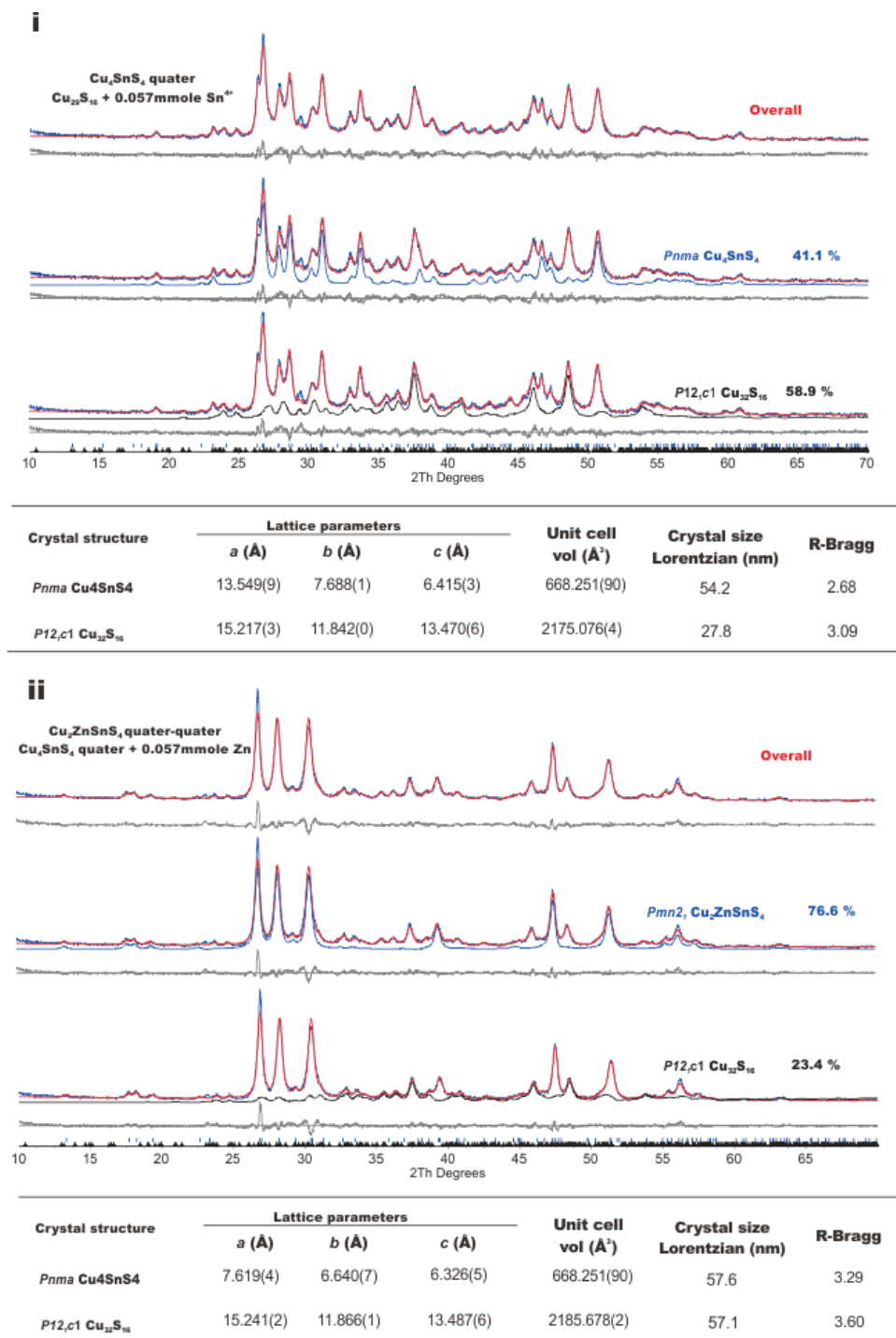

Supplementary Figure 15| (i) Peak fitting of SERS spectrum and **(ii)** XPS characterization of Cu-Sn-S nanoparticles.

Rietveld refinement (**SF14**) of as-synthesized Cu-Zn-Sn-S nanoplates shows the presence of 2 phases. With good fitting to $Pmn2_1$ Cu₂ZnSnS₄ with a fitted lattice parameters of a=7.68 Å, b=6.63 Å, c=6.31 Å and $P2_1/c$ Cu₃₂S₁₆ with a fitted lattice parameters of a=15.29 Å, b=11.86 Å, c=13.45 Å. The fitted CZTS crystal size of ~61 nm correspond well to observe average crystal size from TEM (**SF13**). SERS characterization (**SF15i**) of as-synthesized nanoparticles shows multiple peaks at ~290, 335 and 371 cm⁻¹ corresponding to CZTS phase, 315 cm⁻¹ corresponding to CTS phase and 354 cm⁻¹ corresponding to ZnS phase. while XPS characterization (**SF15ii**) shows the presence of both Cu⁺ and Cu²⁺, Sn²⁺ and Sn⁴⁺, Zn²⁺ ions in the nanoparticles, with the presence of Sn²⁺ described in **SF6**.

14

Sample name	Seed	Moles of Sn precursor	Moles of Zn precursor
CTS$_{half}$	C$_{2-x}$S	1.138×10^{-4}	—
CZTS$_{half-quater}$	CTS$_{half}$	—	0.569×10^{-4}
CTS$_{quater}$	C$_{2-x}$S	0.569×10^{-4}	—
CZTS$_{quater-quater}$	CTS$_{quater}$	—	0.569×10^{-4}

Supplementary Figure 16| Elemental mapping of as-synthesized CTS$_{half}$, CZTS$_{half-quater}$, CTS$_{quater}$ and CZTS$_{quater-quater}$ nanoparticles.

To investigate the preferential growth of CZTS phase from CTS nanoparticles, the amount of Sn to Zn ratio is varied. The elemental distribution of as-synthesized nanoparticles are mapped with EDX to obtain a 2D elemental distribution map (**SF16**). When Sn:Zn is 2:1 (CZTS$_{half-quater}$), we observed the formation of 2 separate population of Cu-S rich phase and hetero Cu-Zn-Sn-S/Cu-Sn-S rich phase. When the Sn:Zn is 1:1 (CZTS$_{quater-quater}$), we observed the formation of 2 separate population of Cu-S rich phase and Cu-Zn-Sn-S rich phase.

Crystal structure	Lattice parameters			Unit cell vol (Å^3)	Crystal size Lorentzian (nm)	R-Bragg
	a (Å)	b (Å)	c (Å)			
$Pnma$ Cu4SnS4	13.549(9)	7.688(1)	6.415(3)	668.251(90)	54.2	2.68
$P12_1c1$ $Cu_{32}S_{16}$	15.217(3)	11.842(0)	13.470(6)	2175.076(4)	27.8	3.09

Crystal structure	Lattice parameters			Unit cell vol (Å^3)	Crystal size Lorentzian (nm)	R-Bragg
	a (Å)	b (Å)	c (Å)			
$Pnma$ Cu4SnS4	7.619(4)	6.640(7)	6.326(5)	668.251(90)	57.6	3.29
$P12_1c1$ $Cu_{32}S_{16}$	15.241(2)	11.866(1)	13.487(6)	2185.678(2)	57.1	3.60

Supplementary Figure S17| Rietveld refinement of **(i)** CTS quarter Cu:Sn 8:1 and (ii) CZTS quarter Cu:Sn:Zn 8:1:1
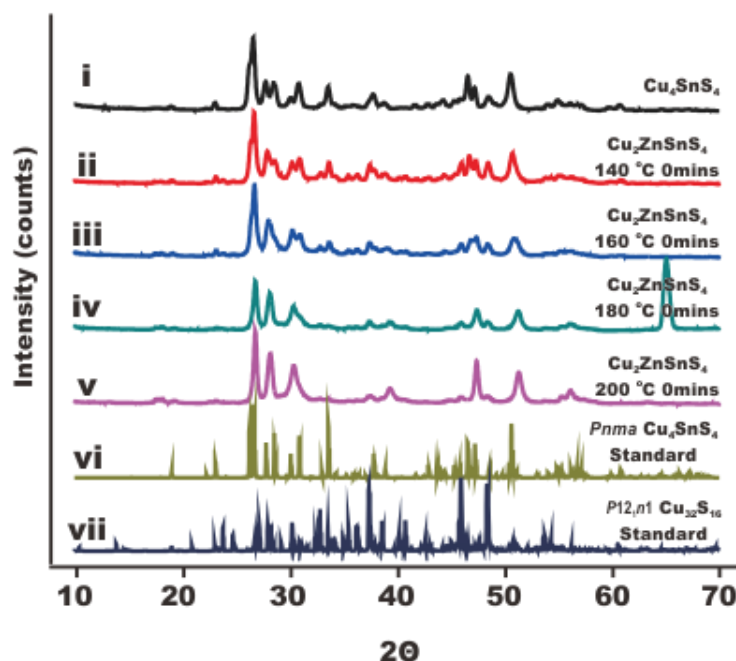
Supplementary Figure S18| XRD spectrum of as-synthesized CZTS nanoparticles after addition of Zn^{2+} into Cu_4SnS_4 nanoparticles solution, heated and immediately quenched upon reaching targeted temperature. **(i)** as-synthesized Cu_4SnS_4 nanoparticles showing crystal phase of *Pnma* Cu_4SnS_4. Solution quenched at **(ii)** 140°C showing crystal phase of *P*12$_1$n1 $Cu_{32}S_{16}$ + *Pnma* Cu_4SnS_4, **(iii)** 160°C 140°C showing crystal phase of *P*12$_1$n1 $Cu_{32}S_{16}$ + *Pnma* Cu_4SnS_4 + wurtzite Cu_2ZnSnS_4, **(iv)** 180°C showing crystal phase of *P*12$_1$n1 $Cu_{32}S_{16}$ + *Pmna* Cu_4SnS_4 + wurtzite Cu_2ZnSnS_4, **(v)** 200°C showing crystal phase of *P*12$_1$n1 $Cu_{32}S_{16}$ + wurtzite Cu_2ZnSnS_4. Standard XRD of **(vi)** *Pnma* Cu_4SnS_4, **(vii)** *P*12$_1$n1 $Cu_{32}S_{16}$.

To determine possible intermediate phase during the growth of CZTS, separate reaction (Cu_4SnS_4 + Zn^{2+}) are carried out with each reaction stopped (quenching in cold water bath) immediately when reaction temperature reached 140 °C, 160 °C, 180 °C, 200 °C and 230 °C respectively. As-synthesized Cu_4SnS_4 nanoparticles show crystal phase of *Pnma* Cu_4SnS_4 (**SF18i**). Nanoparticles obtained from solution quenched at 140 °C (**SF18ii**) shows crystal phase of *P*12$_1$n1 $Cu_{32}S_{16}$ + *Pnma* Cu_4SnS_4, while the nanoparticles quenched at 160 °C (**SF18iii**) shows crystal phase of *P*12$_1$n1 $Cu_{32}S_{16}$ + *Pnma* Cu_4SnS_4 + wurtzite Cu_2ZnSnS_4. When the reaction is quenched at 180 °C (**SF18iv**), the diffractogram shows crystal phase of *P*12$_1$n1 $Cu_{32}S_{16}$ + *Pmna* Cu_4SnS_4 + wurtzite Cu_2ZnSnS_4, while nanoparticles quenched at 200 °C (**SF18v**) showing crystal phase *P*12$_1$n1 $Cu_{32}S_{16}$ + wurtzite Cu_2ZnSnS_4.
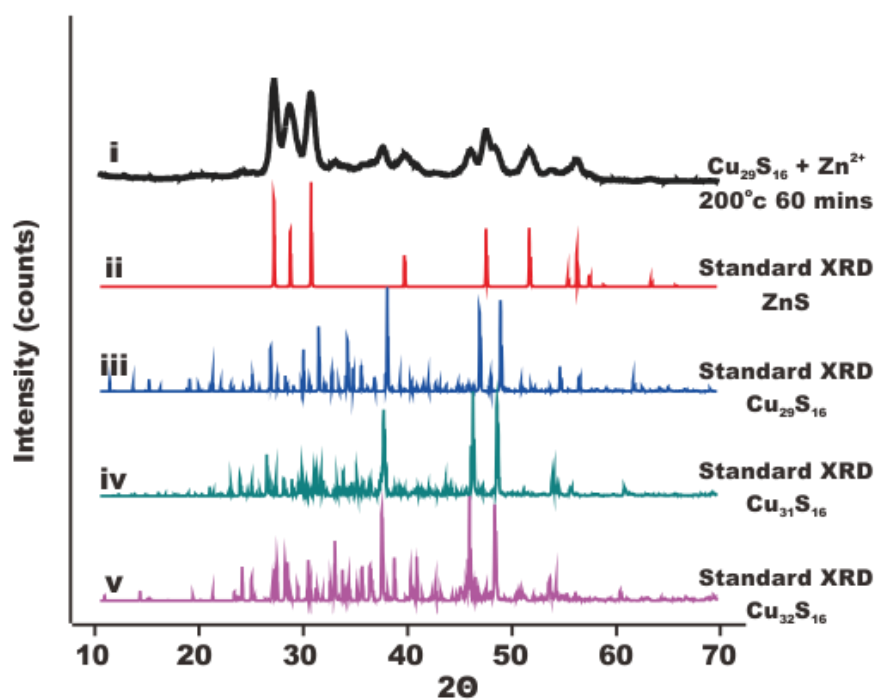
Supplementary Figure 19| XRD of as-synthesized $Cu_{31}S_{16}$/ZnS nanoparticles after reacting $Cu_{29}S_{16}$ with Zn^{2+} at 200 °C for 60 mins.
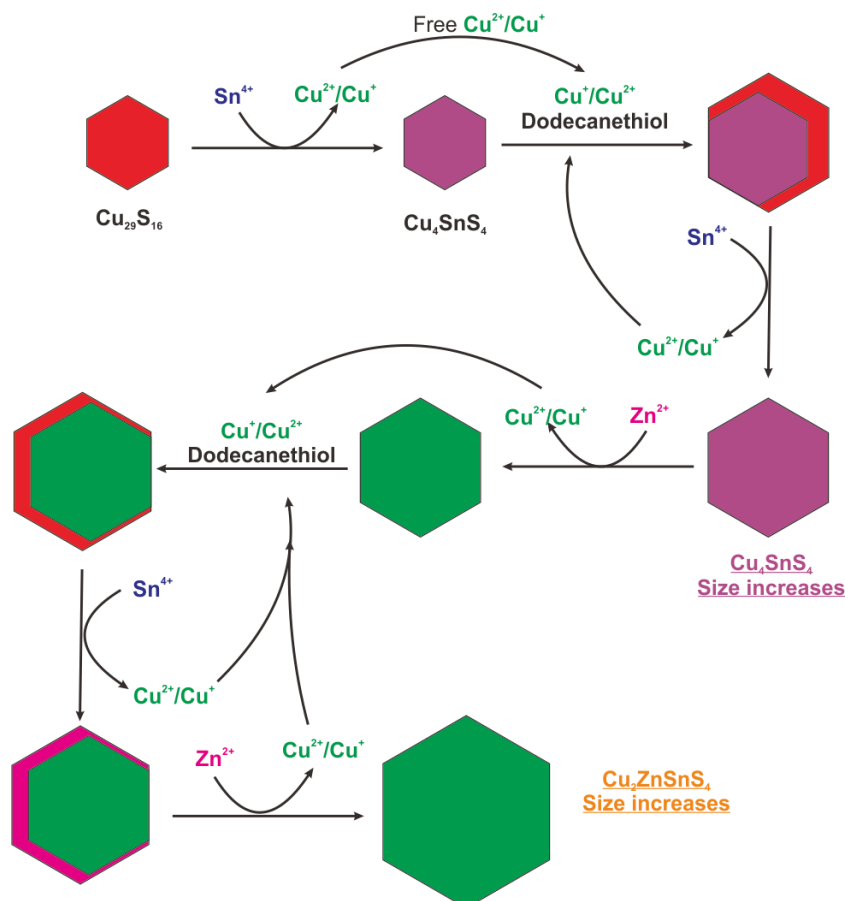
**Supplementary Figure S20|** Pictorial illustration of cation exchange

Supplementary figure S20 shows an pictorial illustration of overall cation exchange taking place. As shown in, Fig 3 and SF22-23, during the displacement of Cu^{2+}/Cu^+ by Sn^{4+} to form Cu_4SnS_4, the displaced Cu^{2+}/Cu^+ react with DDT to form binary Cu-S on Cu_4SnS_4. As time proceed, binary Cu-S phase becomes ternary Cu-Sn-S which caused the growth of Cu_4SnS_4 nanoparticles size to be bigger.

Following on, during the displacement of Cu^{2+}/Cu^+ by Zn^{2+} to form Cu_2ZnSnS_4, the displaced Cu^{2+}/Cu^+ react with DDT to form binary Cu-S on Cu_2ZnSnS_4. As time proceed, binary Cu-S phase becomes ternary Cu-Sn-S and finally to quaternary Cu-Zn-Sn-S which caused the growth of Cu_2ZnSnS_4 nanoparticles size to be bigger.

**a. BF-HRTEM of phase boundary between $Cu_{31}S_{16}$ and Cu_4SnS_4**
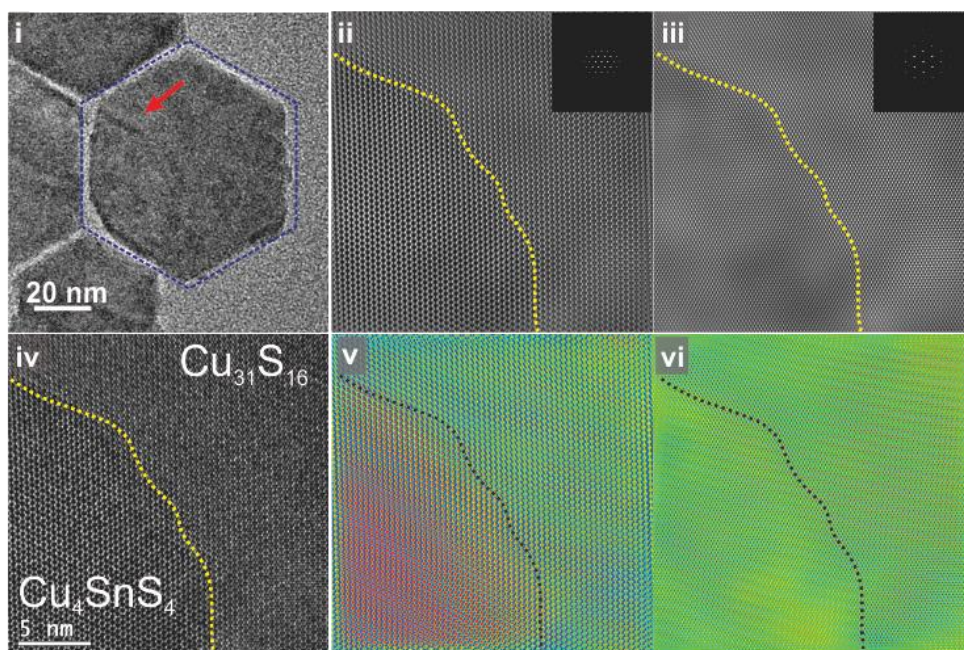
**b. HR HAADF imaging of CTS nanoparticles showing lattice plane of Sn^{4+} overall**
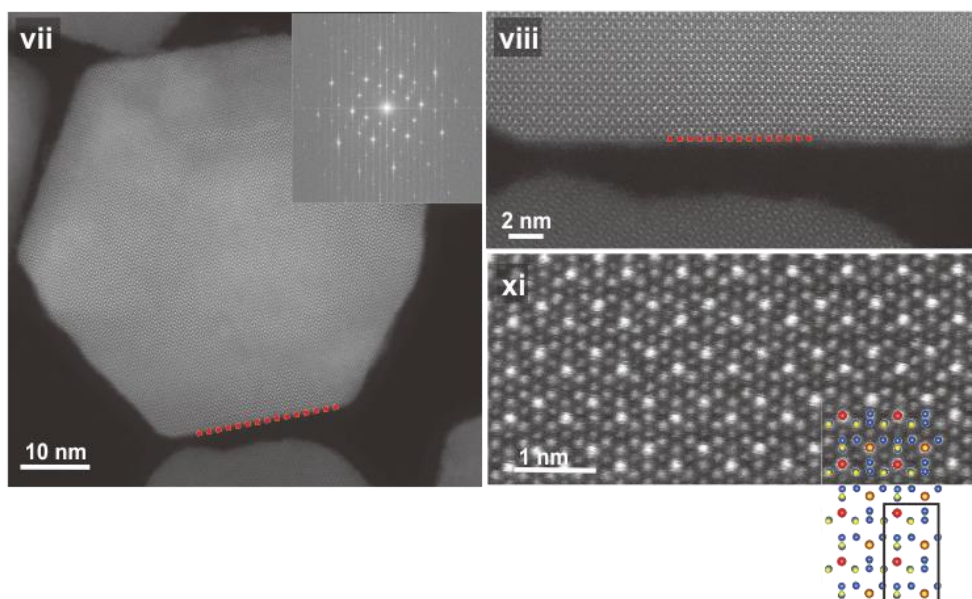
Supplementary Figure 21| a. TEM **(i)** and HRTEM **(iv)** image showing the intermediate phase during transformation of Cu_2S to Cu_4SnS_4. Inverse FFT **(ii)** of **(i)** and false colouration **(v)** emphasizing on Cu_4SnS_4 phase (red contrast) from Cu_2S (blue contrast). Inverse FFT of C_{3v} symmetry hexagonal diffraction pattern **(iii)** of **(i)** and false colouration **(vi)** showing epitaxial hexagonal lattice arrangement between Cu_4SnS_4 and Cu_2S phase. **b.** High resolution HAADF imaging of Cu_2ZnSnS_4/Cu_4SnS_4 nanoparticles showing lattice plane along the side of the nanoparticle with FFT inset **(vii)**, and image at higher magnification **(viii, ix)**.
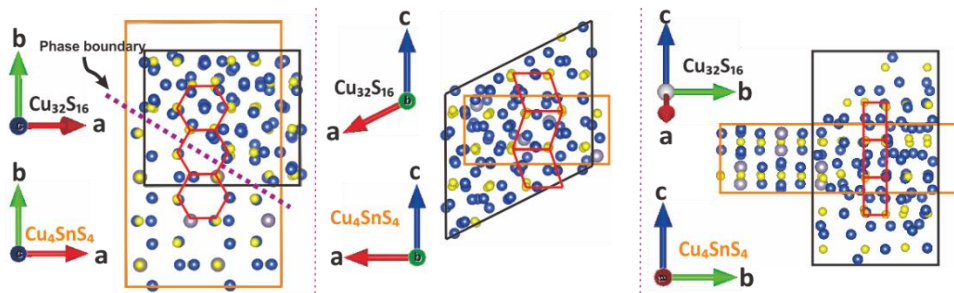
a Proposed epitaxial growth of *P*1 Cu$_{29}$S$_{16}$ into *Pnma* Cu$_4$SnS$_4$ using Sulfur as growth template
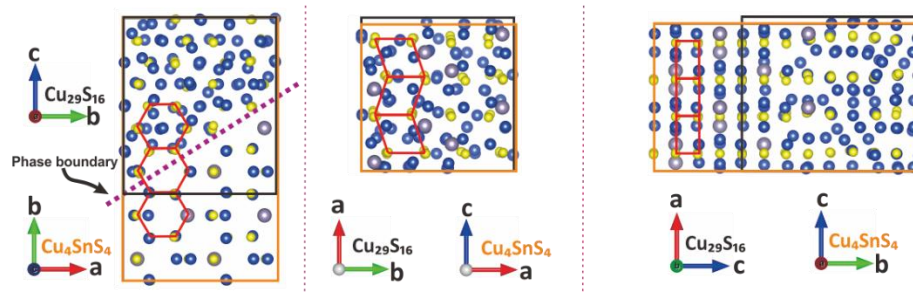
b Proposed epitaxial growth of *P*12$_1$*n*1 Cu$_{31}$S$_{16}$ into *Pnma* Cu$_4$SnS$_4$ using Sulfur as growth template
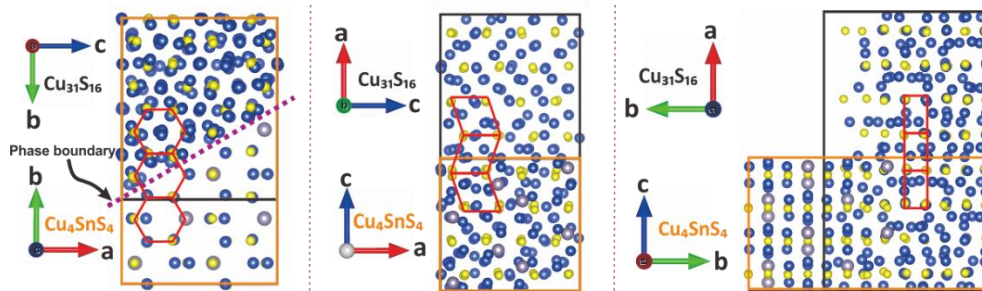
**c** Proposed epitaxial growth of *P*12$_1$*c*1 Cu$_{32}$S$_{16}$ into *Pnma* Cu$_4$SnS$_4$ using Sulfur as growth template

Supplementary Figure 22| Crystal illustration of hetero-nanoparticle interface lattice alignment during growth of Cu$_{29}$S$_{16}$ to Cu$_4$SnS$_4$. **a.** Cu$_{29}$S$_{16}$/Cu$_4$SnS$_4$, **b.** Cu$_{31}$S$_{16}$/Cu$_4$SnS$_4$ and **c.** Cu$_{32}$S$_{16}$/Cu$_4$SnS$_4$.
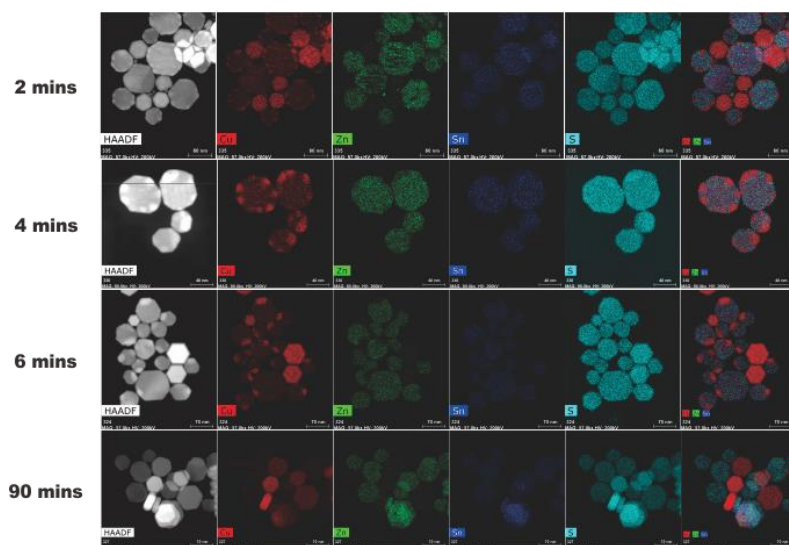
Elemental mapping: Time-growth study of Cu_4SnS_4 to Cu_2ZnSnS_4 0.22 mmole Zn^{2+}
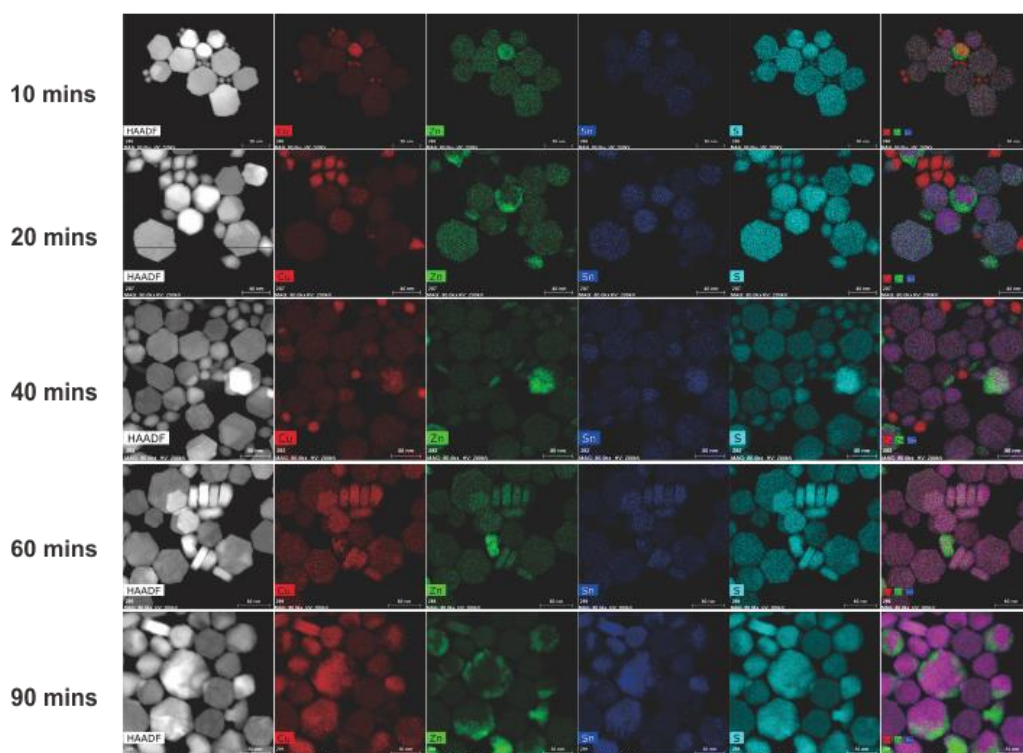
	(atom %)			
	Cu	**Zn**	**Sn**	**S**
10 mins	26.8 ± 2.6	9.8 ± 1.0	14.7 ± 4.5	48.7 ± 4.6
20 mins	25.2 ± 2.4	11.4 ± 1.1	14.1 ± 4.3	49.3 ± 4.6
40 mins	26.2 ± 2.5	10.3 ± 1.0	15.0 ± 4.5	48.5 ± 4.5
60 mins	24.8 ± 2.3	10.5 ± 1.0	15.4 ± 4.7	49.3 ± 4.6
90 mins	26.1 ± 2.6	10.8 ± 1.2	14.1 ± 4.3	49.0 ± 4.7

Supplementary Figure 23| Elemental mapping of nanoparticles obtained during ex-situ study during the growth of Cu_2ZnSnS_4 from Cu_4SnS_4 at 10, 20, 40, 60 and 90 mins.

Time-growth study of Cu_4SnS_4 (quater) to Cu_2ZnSnS_4 0.057 mmole Zn^{2+}

Supplementary Figure 24| Elemental mapping and HR-TEM of nanoparticles obtained during ex-situ study of Cu_2ZnSnS_4 nanoparticles grown from Cu_4SnS_4 **(quarter)** using 0.057 mmol Zn^{2+} **(quarter)**. Elemental distribution change occurring across time 2, 4, 6 and 60 mins.
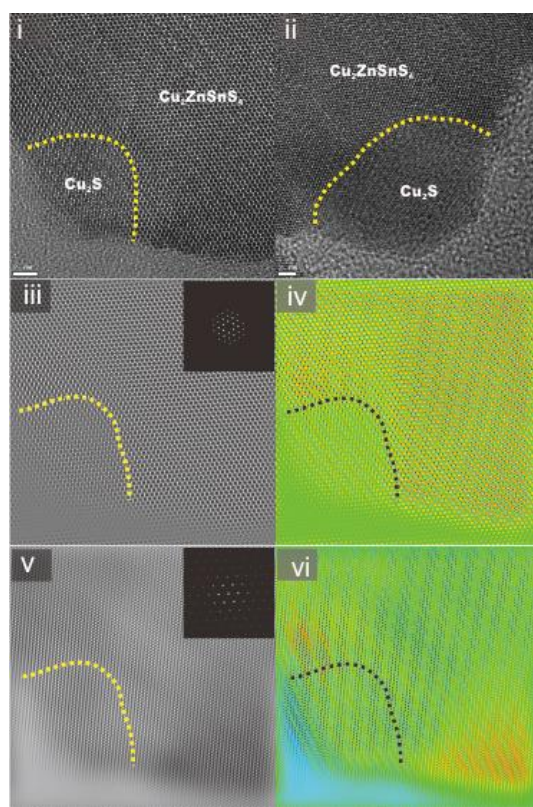
Supplementary Figure 25| (i,ii) HR-TEM image showing the phase boundary between Cu_2ZnSnS_4 and $Cu_{32}S_{16}$ at 2 different corners. **(iii, iv)** Inverse FFT and false colouration of **(i)** emphasizing on Cu_2ZnSnS_4 phase (red contrast) from $Cu_{32}S_{16}$ (green contrast). **(v, vi)** Inverse FFT of C_{3v} symmetry hexagonal diffraction pattern masking and false colouration of **(i)** showing epitaxial hexagonal lattice arrangement between Cu_2ZnSnS_4 and $Cu_{32}S_{16}$ phase.

Crystal: Hexagonal
Space group: $P6_3mc$
$a=b= 3.8387$ Å
$c= 6.3388$ Å

Atom	x	y	z	Occ
S	1/4	2/3	0.3752	1
Cu	1/3	2/3	0	0.5
Zn				0.25
Sn				0.25

<001> axis   **<210> axis**   **<100> axis**
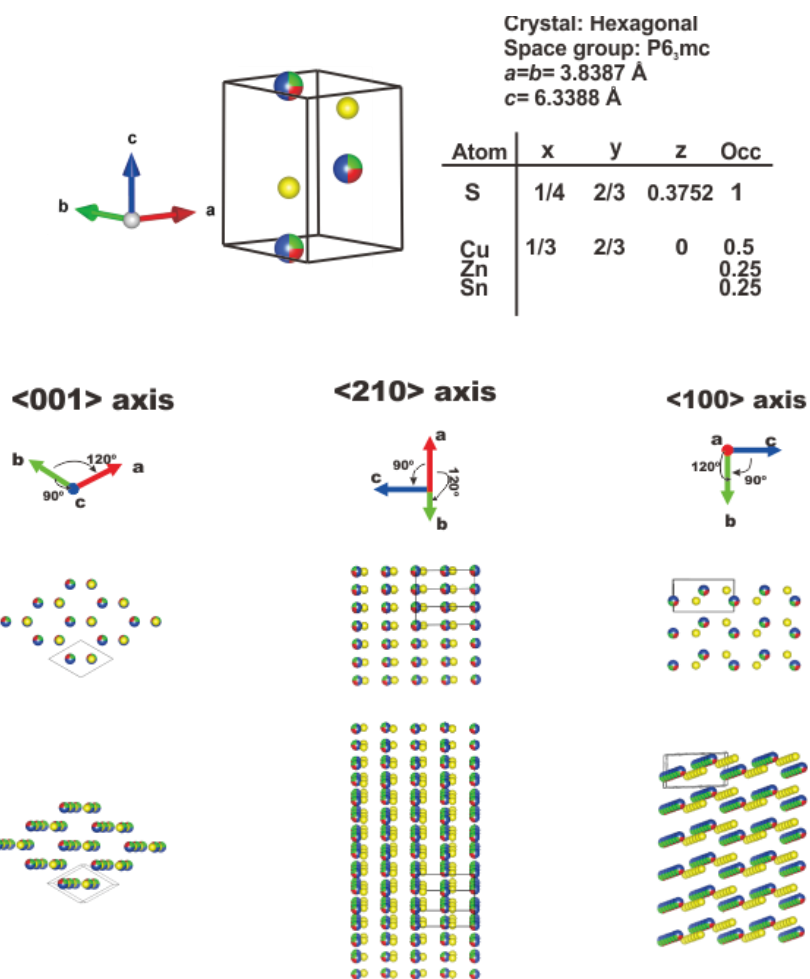
Supplementary Figure S26| 3D crystal illustration of accepted hexagonal wurtzite Cu_2ZnSnS_4 showing the atom arrangements in their respective atomic rows and columns.

Crystal: Orthorhombic
Space group: Pmn2$_1$
a= 7.5385
b= 6.4304
c= 6.2038

Atom	x	y	z	Occ
Cu	1/2	1/3	0	1
Zn	0	0.833	1	1
Sn	0	0.167	1/2	1
S1	1/2	1/3	0.374	1
S2	0	0.167	0.864	1
S3	0	1/3	0.374	1

<001> axis   <010> axis   <210> axis
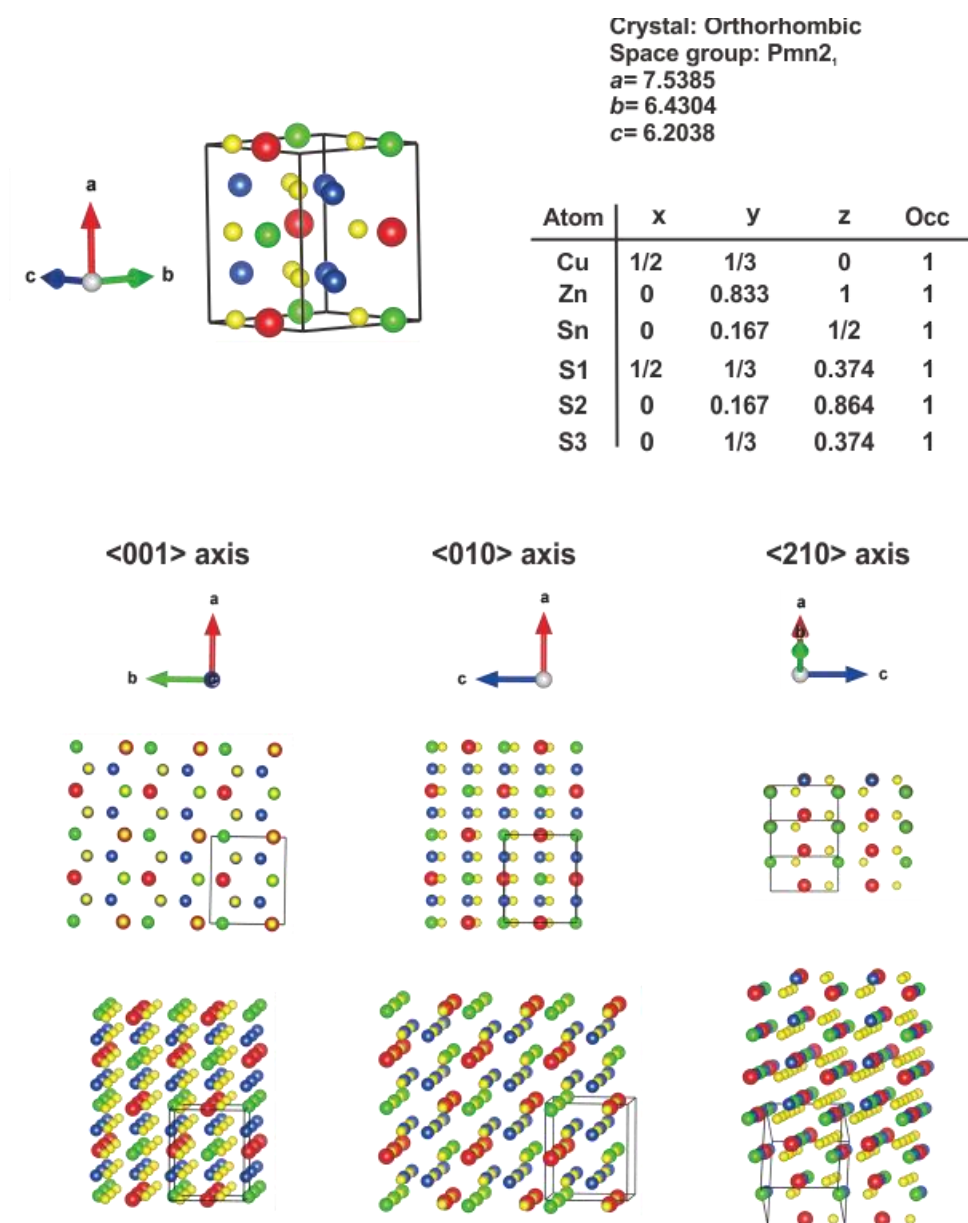
Supplementary Figure S27| 3D crystal illustration of accepted orthorhombic Cu$_2$ZnSnS$_4$ showing the atoms arrangement in their atomic rows and columns.

25

Crystal: Monoclinic
Space group: *Pc*
a = 7.5385
b = 6.4304
c = 6.2038

Atom	x	y	z	Occ
Cu1	0.752	0.829	0.501	1
Cu2	0.252	0.498	0.001	1
Cu3	0.499	0.998	0.001	1
Cu4	0.999	0.329	0.501	1
Zn1	0.750	0.495	0.997	1
Zn2	0.250	0.832	0.497	1
Sn1	0.500	0.331	0.498	1
Sn2	1.000	0.995	0.998	1
S1	0.762	0.504	0.371	1
S2	0.737	0.827	0.864	1
S3	0.262	0.823	0.871	1
S4	0.237	0.500	0.364	1
S5	0.495	0.329	0.887	1
S6	0.996	0.998	0.387	1
S7	0.504	0.984	0.365	1
S8	0.004	0.343	0.865	1
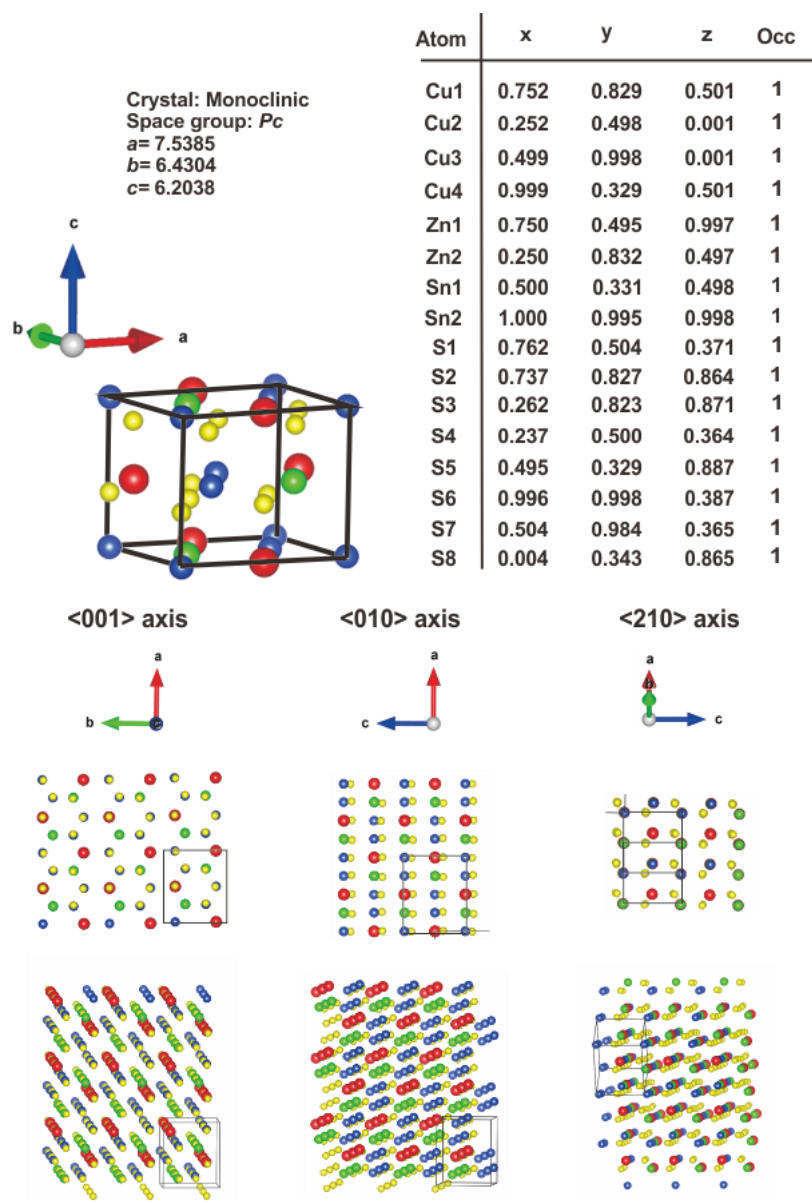
Supplementary Figure S28| 3D crystal illustration of accepted monoclinic Cu_2ZnSnS_4 showing the atom arrangements in their respective atomic rows and columns.

Supplementary Table 1. The *k*-mesh setting, calculated lattice parameters and formation entropy energies per unit formular of different intermediate compounds by PBE functional. The values in parentheses are experimental results.

Compounds	Atoms in supercell	k-mesh setting	Lattice parameters			Total energy(eV)	Ref
			a(Å) Calculated (*Literature*)	b(Å) Calculated (*Literature*)	c(Å) Calculated (*Literature*)		
$Cu_{29}S_{16}$(**P1**)	180	2×2×2	13.341(*13.409*)	13.530(*13.405*)	15.617(*15.485*)	-719.9440	31
$Cu_{31}S_{16}$(**P2₁/n**)	376	1×1×1	26.731(*26.897*)	15.930(*15.745*)	13.519(*13.565*)	-1507.5852	34
$Cu_{32}S_{16}$(**P2₁/c**)	144	1×1×1	14.996(*15.246*)	12.163(*11.884*)	13.412(*13.494*)	-574.1400	34
Cu_4SnS_4(**Pnma**)	36	2×4×4	13.622(*13.558*)	7.702(*7.681*)	6.492(*6.412*)	-150.0604	35

Supplementary Table 2. DFT calculated enthalpy* of phase formation

Phase	$Cu_{29}S_{16}$	$Cu_{31}S_{16}$	Cu_2S	Cu_4SnS_4	Cu_2ZnSnS_4	
Space group	*P1*	*P12₁n1*	*P12₁c1*	*Pnma*	*Pc*	*Pmn2₁*
ΔH_f* (eV)	-5.666	-6.656	-0.366	-2.242	-3.673	-3.663

*$\Delta H_f = E_{soild} - n_\alpha \sum_\alpha E_\alpha^{bulk} \leq n_\alpha \Delta\mu_\alpha \leq 0$, where where μ_α is the chemical potential of element α during reaction, μ_α^0 is the reference chemical potential of element α in its standard elemental phase (e.g fcc-Cu$_{(s)}$, fcc-Zn$_{(s)}$), $\Delta\mu_\alpha$ is the change in free energy due to the state and chemical environment of element α during reaction

Supplementary Table 3. Calculated lattice parameters of CZTS with different geometric structures and energy differences with respect to ZB-KS structure by PBE functional.

	Zinc-Blende derived			Wurtzite derived	
	ZB-ST[3]	ZB-ST[4]	PMCA	WZ-ST[5]	WZ-KS[6]
Energy differences (eV)	0	0.046	0.060	0.135	0.114
Theoretical lattice parameters (Å)	$a=b=5.468$	$a=b=5.462$	$a=b=5.464$	$a=7.693$	$a=7.720$
	$c=10.939$	$c=10.962$	$c=10.956$	$b=6.685$	$b=6.672$
				$c=6.362$	$c=6.360$
Experimental lattice parameters (Å)	$a=b=5.428$	$a=b=5.436$	-	$a=7.539$	$a=7.637$
	$c=10.856$	$c=10.872$		$b=6.430$	$b=6.614$
				$c=6.204$	$c=6.298$

ZB= Zinc-blende, KS=Kesterite, ST=Stannite, PMCA=Primitive-mixed CuAu-like, WZ=wurtzite

Reference

1.   Liu, Y.; Yao, D.; Shen, L.; Zhang, H.; Zhang, X.; Yang, B., Alkylthiol-Enabled Se Powder Dissolution in Oleylamine at Room Temperature for the Phosphine-Free Synthesis of Copper-Based Quaternary Selenide Nanocrystals. *J. Am. Chem. Soc.* **2012,** *134*, 7207-7210.
2.   Chesman, A. S. R.; Duffy, N. W.; Peacock, S.; Waddington, L.; Webster, N. A. S.; Jasieniak, J. J., Non-injection synthesis of Cu2ZnSnS4 nanocrystals using a binary precursor and ligand approach. *RSC Advances* **2013,** *3*, 1017-1020.
3.   Schorr, S.; Hoebler, H.-J.; Tovar, M., A neutron diffraction study of the stannite-kesterite solid solution series. *Eur. J. Mineral.* **2007,** *19*, 65-73.
4.   ZHANG, J.; Lexi, S.; Yujun, F.; Erqing, X., Cu 2 ZnSnS 4 thin films prepared by sulfurization of ion beam sputtered precursor and their electrical and optical properties. *Rare Metals* **2006,** *25*, 315-319.
5.   Jiang, H.; Dai, P.; Feng, Z.; Fan, W.; Zhan, J., Phase selective synthesis of metastable orthorhombic Cu 2 ZnSnS 4. *J. Mater. Chem.* **2012,** *22*, 7502-7506.
6.   Regulacio, M. D.; Ye, C.; Lim, S. H.; Bosman, M.; Ye, E.; Chen, S.; Xu, Q. H.; Han, M. Y., Colloidal nanocrystals of Wurtzite‐type Cu2ZnSnS4: facile noninjection synthesis and formation mechanism. *Chemistry‐A European Journal* **2012,** *18*, 3127-3131.